Nanoscale Manipulation of Spinel Lithium Nickel Manganese Oxide Surface by Multisite Ti Occupation as High-Performance Cathode

Biwei Xiao, Hanshuo Liu, Jian Liu, Qian Sun, Biqiong Wang, Karthikeyan Kaliyappan, Yang Zhao, Mohammad Norouzi Banis, Yulong Liu, Ruying Li, Tsun-Kong Sham, Gianluigi A. Botton, Mei Cai, and Xueliang Sun**

A novel two-step surface modification method that includes atomic layer deposition (ALD) of TiO_2 followed by post-annealing treatment on spinel $LiNi_{0.5}Mn_{1.5}O_4$ (LNMO) cathode material is developed to optimize the performance. The performance improvement can be attributed to the formation of a $TiMn_2O_4$ (TMO)-like spinel phase resulting from the reaction of TiO_2 with the surface LNMO. The Ti incorporation into the tetrahedral sites helps to combat the impedance growth that stems from continuous irreversible structural transition. The TMO-like spinel phase also alleviates the electrolyte decomposition during electrochemical cycling. 25 ALD cycles of TiO_2 growth are found to be the optimized parameter toward capacity, Coulombic efficiency, stability, and rate capability enhancement. A detailed understanding of this surface modification mechanism has been demonstrated. This work provides a new insight into the atomic-scale surface structural modification using ALD and post-treatment, which is of great importance for the future design of cathode materials.

The growing demand for renewable energy has stimulated the development of lithium-ion batteries (LIBs), which are deemed as the key component for the next-generation electric and hybrid electric vehicles. LIBs with high energy density are therefore extremely desirable in these high power devices.[1] Cathode materials that operate over 4.5 V (vs Li/Li^+) with high energy density are considered as the superlative candidates to replace the currently commercialized $LiCoO_2$, which is restricted to portable devices such as cell phones and laptops. Among these high-voltage cathode materials, $LiNi_{0.5}Mn_{1.5}O_4$ (LNMO) with a spinel structure holds great potential in terms of natural elemental abundance, high operating voltage (4.7 V), and theoretical capacity (147 $mAhg^{-1}$).[2,3] Nevertheless, such high operating voltage of LNMO involves surface chemistry issues such as irreversible surface phase transition, transition metal dissolution, Jahn–Teller distortion of Mn^{3+}, electrolyte oxidation, etc.[4–10] Considerable efforts have been devoted to alleviating these deficiencies by coating the LNMO surface using metal oxides,[11–13] phosphates,[14–17] fluorides,[18,19] and so forth. These coating materials can tackle the metal dissolution, electrolyte decomposition, and Mn^{3+} Jahn–Teller distortion problems by simply shielding the cathode material from direct exposure to the electrolyte. Bulk doping during materials preparation is another strategy aimed at suppressing the phase transition in LNMO,[20–26] but the excessive and uncontrollable doping will block the Li ions transportation channels in its bulk structure, leading to active capacity loss.[27–29]

Considering the fact that side reactions predominantly happen on the surface of LNMO due to the unbalanced Li ions mobility on the boundary especially at high current densities,[30] restricting the controllable doping modification within the surface turns out to be a feasible and promising approach. In previous studies, metal oxides or phosphates were often deposited onto the surface of cathode materials by a sol-gel method followed by annealing. During the post-annealing process, the metal ions (Mg^{2+}, Al^{3+}, etc.) diffuse into the surface lattices and help improve the performance of the electrode materials by: (1) eliminating the onset of Jahn–Teller distortion of transition metals such as Mn^{3+}; (2) suppressing the transition metals dissolution; (3) preventing severe electrolyte oxidative decomposition; (4) combating second phase formation; (5) strengthening the metal–oxygen bonds on the surface; and (6) changing the surface basicity.[30–36] However, manipulating the doping amount and uniformity by these methods has yet remained to be unresolved due to the difficulty in realizing uniform and

Dr. B. Xiao, Dr. J. Liu, Dr. Q. Sun, B. Wang, Dr. K. Kaliyappan, Y. Zhao, Dr. M. N. Banis, Y. Liu, R. Li, Prof. X. Sun
Department of Mechanical and Materials Engineering
University of Western Ontario
London, ON N6A 5B9, Canada
E-mail: xsun@eng.uwo.ca

Dr. H. Liu, Prof. G. A. Botton
Department of Materials Science and Engineering
McMaster University
Hamilton, ON L8S 4L8, Canada
E-mail: gbotton@mcmaster.ca

B. Wang, Prof. T.-K. Sham
Department of Chemistry
University of Western Ontario
London, ON N6A 5B7, Canada

Dr. M. Cai
General Motors Research and Development Center
Warren, MI 48090-9055, USA

The ORCID identification number(s) for the author(s) of this article can be found under https://doi.org/10.1002/adma.201703764.

DOI: 10.1002/adma.201703764

thin coating by conventional methods, also, there is a lack of solid evidence on the doping mechanisms and the structure change upon such treatment. Atomic layer deposition (ALD) is an emerging technique that is capable of depositing conformal and uniform thin films, and has been extensively used to coat the surface of cathode materials with ultrathin layers for the purpose of improving their electrochemical performance in LIBs.[37–39] Therefore, ALD provides a feasible approach to tailoring the uniformity and amount of surface doping on the cathode materials by easily controlling the thickness of the uniform coating layers. However, the adoption of the combination of ALD and post-treatment to design the surface composition of cathode materials is scarcely reported.

In this work, we successfully modified the surface structures of LNMO particles by post-annealing ALD derived TiO_2 with different thicknesses. Part of the Ti was found to diffuse into the 8a tetrahedral sites which were previously occupied by lithium atoms, creating a uniform layer of $TiMn_2O_4$ (TMO)-like cation deficient spinel phase. Besides, more Ti atoms were found to have diffused into the bulk of the LNMO and resulted in octahedral site doping. The Ti incorporation suppresses the surface phase transformation that could result in impedance build-up as observed during the first charge process, thereby benefiting the discharge capacity from the initial cycle. These synergetic effects help build a surface layer with desired thickness comprising both moderate electrical and ionic conductivity and contributing to increased capacity and stability. Moreover, it was also found that the thickness of the TiO_2 coating layer should be carefully adjusted in order to minimize the formation of impurities such as the $Li_xNi_{1-x}O$ in the rock salt phase, which could jeopardize the battery performance. It was found that TiO_2 coating deposited with 25 ALD cycles (≈2 nm in thickness) was optimal, whereas thinner or thicker TiO_2 coatings were either inadequate to make desirable difference or excessive that leads to noticeable drop in performance. The comparison between the pure TiO_2-coated LNMO and annealed TiO_2-coated LNMO samples revealed that the post-annealing process is crucial for achieving an optimal battery performance.

The ratio of Li:Ni:Mn of the as-purchased LNMO was identified to be 1.02:0.49:1.50 through inductively coupled plasma measurement, which is very close to the theoretical stoichiometry of 1:0.5:1.5. The morphologies of the LNMO/$n$$TiO_2$ samples were characterized using scanning electronic microscopy (SEM) and the typical images are shown in **Figure 1**. The bare LNMO particles show very smooth surfaces with well-defined edges (Figure 1a). Each primary LNMO particle has a spherical shape with a diameter of around 10–20 µm and is composed of many secondary particles of around 500 nm (Figure S2, Supporting Information). Comparing with the bare LNMO, the LNMO/25TiO_2 particles shown in Figure 1b present slightly rougher surfaces, due to the presence of TiO_2 layer. The TiO_2-coated particles show a noticeable morphology change after post-annealing treatment. Smaller particles (around 50 nm) appear on the surface, and their density is very high on the LNMO/250TiO_2A sample. The occurrence of such particles suggests that the TiO_2 layer underwent some changes during post-annealing process, which will be discussed in following sections.

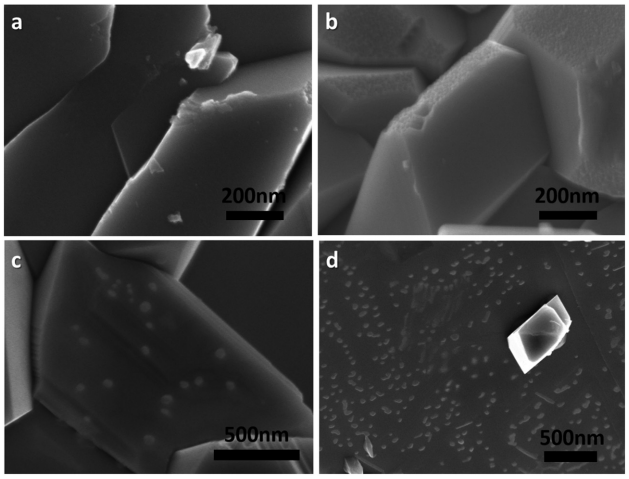

Figure 1. SEM images of a) bare LNMO, b) LNMO/25TiO_2, c) LNMO/25TiO_2A, and d) LNMO/250TiO_2A.

The TiO_2 deposition via ALD has been characterized by electron energy-loss spectroscopy (EELS) mapping of the LNMO/250TiO_2 sample. As can be seen from the EELS spectra in **Figure 2**b, only Ti and O are observed at the outermost layer suggesting that a TiO_2 layer has been deposited onto the LNMO particle. The Ti L-edge is still visible when approaching into the bulk of the particle, where Mn and Ni L-edges show up. Since the data collected from each region of interest (ROI) is a 3D projection of that region from the sphere (particle), the EELS spectrum acquired from the bulk region as marked in Figure 2b is actually a projection of the whole particle. Therefore, the observation of Ti from the bulk ROIs indicates that the whole LNMO surface is well covered by the TiO_2 coating. The sample with 250 ALD cycles shows a surface TiO_2 layer with the thickness of about 5–10 nm among different particles. In addition, the O K-edge in the metal oxide mainly corresponds to the transition of the O 1s state to the O 2p state which is hybridized with the transition metal 3d and 4sp orbitals.[40] The peak shape does not show significant change from the surface to the bulk, indicating that the O atoms are simply present in the forms of TMO_6 octahedra in TiO_2 and LNMO.

The structures of the samples were investigated by X-ray diffraction (XRD), as shown in **Figure 3**a. The bare LNMO can be well indexed to the cubic spinel structure with an $Fd\bar{3}m$ space group, in which Mn and Ni randomly occupy the octahedral 16d sites, O occupies the 32e sites, and Li occupies the tetrahedral 8a sites.[2] The presence of oxygen vacancies leads to the existence of Jahn–Teller active Mn^{3+}.[41] No TiO_2 peaks can be found in the LNMO/250TiO_2 sample, most likely due to the thin and amorphous nature of the TiO_2 layer. However, significant difference can be observed on the LNMO/250TiO_2A sample. Some new peaks emerged in the XRD pattern of LNMO/250TiO_2A. Impurity rock salt phase $Li_xNi_{1-x}O$ peaks at $2\theta \approx 37°$, 43°, and 64° marked with "+" symbol appeared on the XRD patterns.[42,43] Peaks marked with "↓" are indexed to the TMO-like spinel phase, more details regarding this phase will be discussed below. Figure 3b shows an enlarged degree range between 43.5° and 45°, in which the peak of LNMO/250TiO_2A sample clearly shows a shift to lower angle. This shift suggests

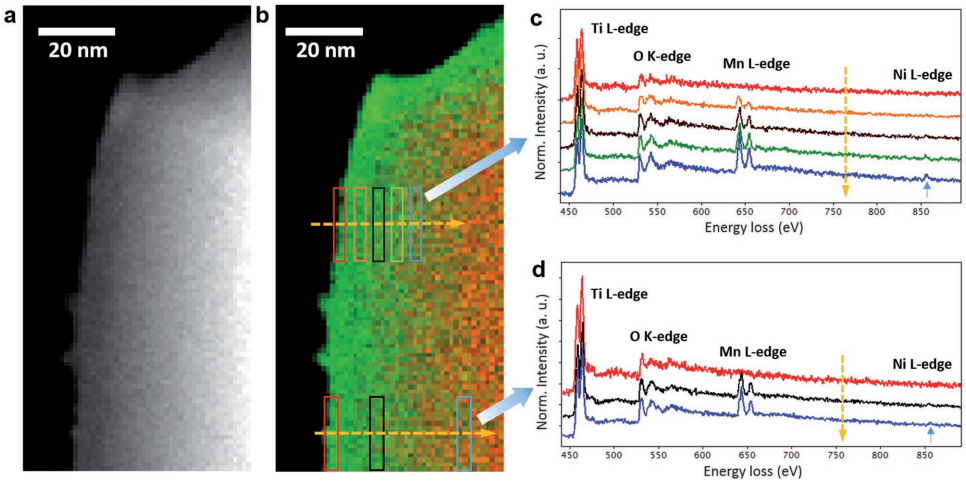

Figure 2. EELS map taken from a LNMO/250TiO_2 particle. a) HAADF-STEM image of the LNMO/250TiO_2 particle. b) EELS map for the LNMO/250TiO_2 particle (Ti: green; Mn: red). c,d) EELS spectra integrated from the corresponding areas shown in (b).

that part of the Ti has doped into the LNMO lattice and resulted in slight lattice parameter change.

A structural change is observed near the surface of the TiO_2-coated LNMO particle after post heat-treatment. **Figure 4**a shows the high-angle annular dark field scanning transmission electron microscopy (HAADF-STEM) image of a LNMO/250TiO_2A particle from the surface to the bulk. The bulk of the particle maintains the LiM_2O_4-type $Fd\overline{3}m$ spinel structure (M = Mn and Ni), as shown in the corresponding HAADF-STEM image (Figure 4c) viewing along the [101] zone axis, with Li occupying the 8a tetrahedral sites and transition metal atoms occupying the 16d octahedral sites. Note that the bright atomic columns seen in the HAADF image are the transition metal atom, while the light elements are not visible from the image. Figure 4g shows a simulated HAADF image in the [101] zone projection of the LiM_2O_4 phase which is consistent with the experimental data. Interestingly, a noticeable change in the intensity of Li sites is observed near the particle surface, which becomes brighter and visible, indicating that the Li tetrahedral sites are occupied by heavier transition metal atoms. A high-resolution HAADF-STEM image representing the surface structure is shown in Figure 4b with the corresponding filtered image shown in Figure 4d that enables a clearer view of the atomic arrangement. This near-surface lattice can be indexed to the [101] zone axis of a TMO-like spinel phase with transition metal occupying both the octahedral and tetrahedral sites. The simulated HAADF image of the TMO phase is in good agreement with the experimental data, as shown in Figure 4f. It should be noted that the high-resolution transmission electron microscopy (HRTEM) image of LNMO/25TiO_2-A has also been acquired and shown in Figure S3b (Supporting Information), a second phase has also been observed, the energy-dispersive X-ray spectroscopy (EDX) mapping of the surface shown in Figure S7 (Supporting Information) also indicated the enrichment of Ti.

The coordination environment of Ti before and after annealing is further evaluated by the Ti K-edge X-ray absorption

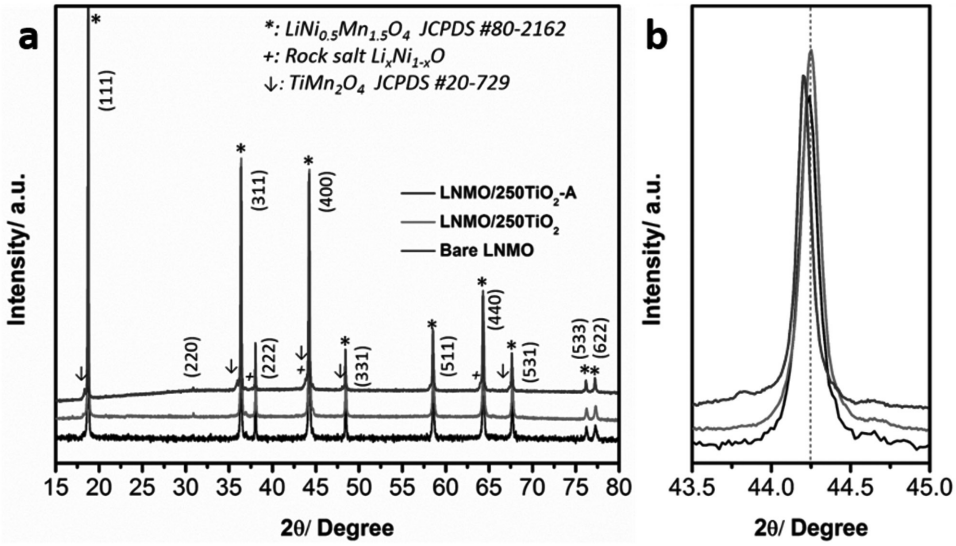

Figure 3. XRD patterns of a) bare LNMO, LNMO/250TiO_2, and LNMO/250TiO_2A and b) enlarged region from 43.5° to 45.0°.

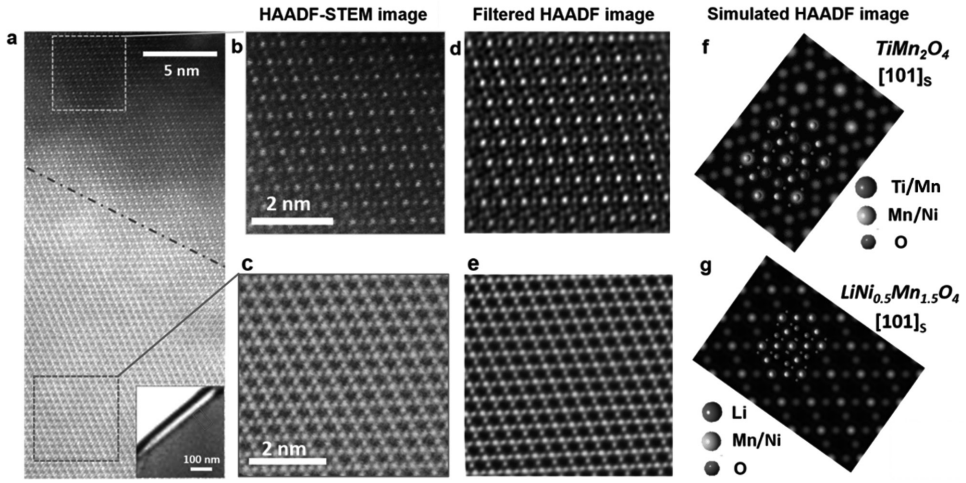

Figure 4. a) HAADF-STEM image of LNMO/250TiO_2A particle acquired near the surface, the corresponding region is shown in the inset image. b,c) Atomic-resolution HAADF-STEM images showing the lattice structure of the outermost layer and the inner region of the particle, respectively. d,e) Processed images corresponding to the HAADF-STEM images shown in (b) and (c) with a band-pass filter applied. f,g) Simulated HAADF images of $LiMn_2O_4$ and $TiMn_2O_4$.

near-edge structure (XANES) collected from LNMO/250TiO_2 and LNMO/250TiO_2A samples. **Figure 5**a shows the XANES data collected in fluorescence yield (FLY) mode, which has a detection depth of up to 100 nm, so that one can obtain the information from the subsurface region of the material.[44,45] The as-deposited LNMO/250TiO_2 shows a typical amorphous TiO_2 spectra with a broad feature.[46] However, upon post-annealing, the main edge became well-resolved and two clearly identifiable peaks, namely, A_1 and A_2 arose in the pre-edge region (as shown in the inset in Figure 5a). Pre-edge features in Ti K-edge XANES are always employed as an indication of the Ti coordination numbers since these 1s–3d quadruple transitions are very sensitive to the local environment in terms of symmetry and coordination number.[46] A_1 is normally assigned to the octahedral Ti^{4+}, which has a dipole-forbidden 1s–3d t_{2g} transition, while peak A_2 is generally attributed to the transition of the 1s electron into hybridized Ti 3d/4p states, which has an e_g symmetry. As has been suggested by Miiller and co-workers, the intensity of the A_2 peak is correlated to the coordination number since it originates from the Ti 3d/4p coordination.[47] A higher A_2 peak gives rise to the lower coordination number, that is, more tetrahedral Ti^{4+}.[46] A scrutiny of the spectra features also reveals that the Ti K-edge XANES in the LNMO/250TiO_2A sample differs from the Ti K-edge of either rutile or anatase TiO_2 as shown in Figure S11a (Supporting Information). The extra pre-edge peak appearing at higher energy than the A_2 peak (≈4975 eV) in TiO_2 XANES is attributed to the transition of 1s electron into 3d states of adjacent Ti^{4+} cations and its intensity is proportional to the coordination number.[47] The disappearance of this peak in the Ti K-edge XANES of the LNMO/250TiO_2A sample indicates that some of the Ti^{4+} ions occupy the tetrahedral sites where Li ions resided previously. Generally, Ti^{4+} is hardly found to occupy the tetrahedral sites, but exceptions have been observed when Ni^{2+} is presented in the spinel, Ni^{2+} has high octahedral site preference due to the high crystal field stabilization energy (CFSE), whereas Ti^{4+} has no preference because it has an empty 3d orbital (see Figure S6, Supporting Information, for details).[48] Therefore, the presence of Ni^{2+} in $LiNi_{0.5}Mn_{1.5}O_4$ might also explain why only octahedral coordinated Ti was found in the case of surface Ti doping of $LiMn_2O_4$ as reported by Amine and co-workers.[49] In addition, part of the Ti^{4+} ions are octahedrally coordinated, indicating that the Ti has replaced part of the Mn/Ni in the bulk and formed a $LiTi_xNi_yMn_{2-x-y}O_4$ phase, which complies well with the peak shift observed in the XRD results. This could be ascribed to the fact that squeezing into a tetrahedral site requires more energy than octahedral site due to size effect, energy tend to dissipate as the depth increases. Partial occupation of Ti in the octahedral sites of TMO-like phase may also be a possible explanation for the A_1 peak.

In addition, the new phase is further confirmed by the EELS spectrum acquired from the surface region of the LNMO/250TiO_2A particle, as shown in Figure 5c. Both Ti and Mn are observed from the surface region with a small amount of coexisting Ni, which is consistent with the surface structural indexation of the TMO-like spinel phase as shown in Figure 4. Furthermore, a significant change in the Li K-edge is observed from the bulk to the surface of the annealed particle. The intensive Li K-edge presents in the bulk is not detected in the surface layer, as shown in Figure 5b, indicating that the surface TMO-like spinel phase formed after annealing contains almost no Li. According to EELS quantification, the Ti concentration (≈7%) in the surface region is lower compared to the ideal TMO phase, indicating that there would be vacancies on the tetrahedral sites. The Ti concentration decreases dramatically when approaching from the outermost surface to the bulk, whereas a weak Ti L-edge signal is still observed beyond 40 nm depth, suggesting that the diffusion of Ti is rather vigorous under such post-annealing conditions. Besides, the Mn L-edge acquired from the bulk to the surface exhibits a clear chemical shift of ≈3 eV toward lower energy and the L_3/L_2 ratio of the Mn L-edge decreases dramatically. It is generally accepted that the energy shift and the relative intensity of the two peaks in Mn L-edge are correlated with

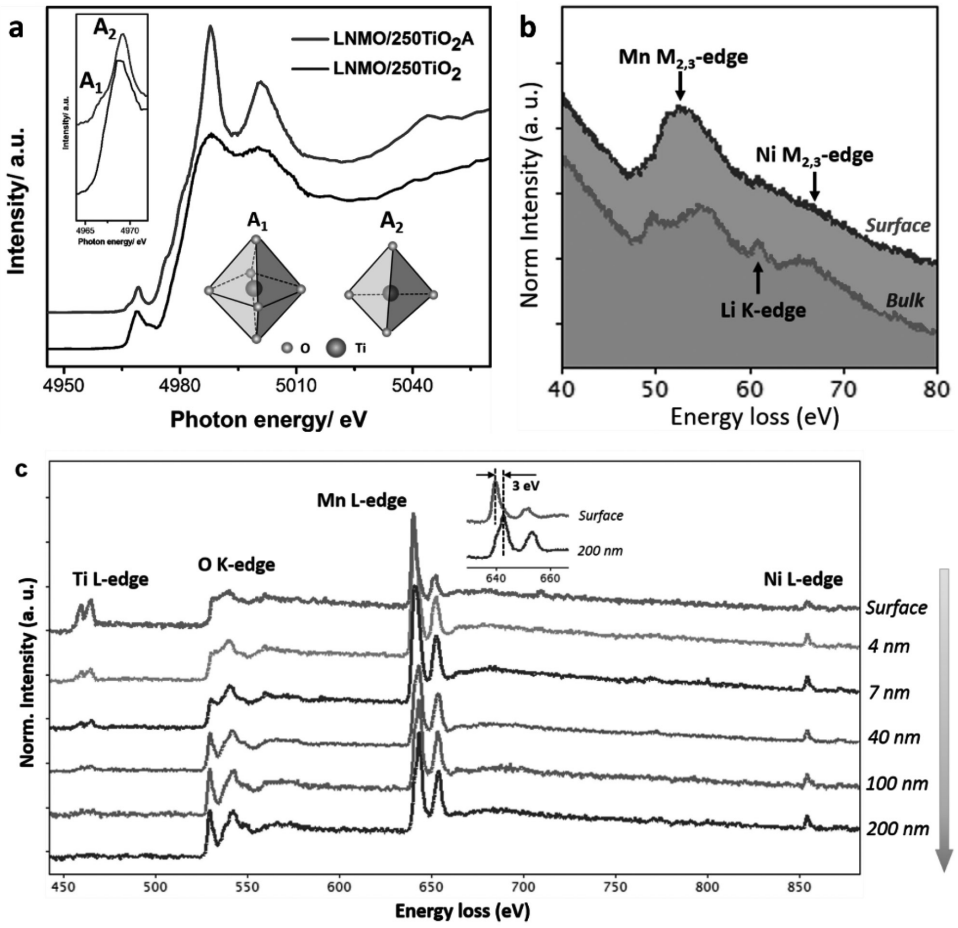

Figure 5. a) XANES spectra of Ti K edges of LNMO/250TiO_2 and LNMO/250TiO_2A collected at FLY mode (inset: enlarged pre-edge regions; schematics showing tetrahedral and octahedral Ti); b) EELS spectra of the Mn M-edge and Li K-edge on the surface and bulk (without background subtraction); c) EELS depth profile of the LNMO/250TiO_2A particle from the surface to the bulk.

the oxidation state of Mn ions.[50,51] Therefore, it can be concluded from the spectra that the oxidation state of the Mn from the bulk to the surface varies, with predominantly Mn^{2+} near the surface and Mn^{3+}/Mn^{4+} in the bulk. The reduction of Mn ions can be ascribed to the charge balance with the incorporation of Ti^{4+}.[50] The O K-edge EELS spectra are also shown in Figure 5c. It is noticed that the peak features of the O K-edge vary greatly when approaching the surface. It has been reported that the reduction of transition metals will result in an intensity decrease of the O pre-edge since the O 2p state is highly hybridized with the transition metal 3d states,[40] thus the significant drop of the O pre-peak is consistent with the Mn reduction observed from the Mn L-edge. The O K-edge feature resembles a TiM_2O_4 (M = metals) O K-edge as has been reported by Fleet and co-workers.[52]

The above observations clearly indicate that TiO_2 was deposited onto the surface of LNMO particle with controlled thickness and that upon post-annealing treatment, part of the Ti substituted the surface Li in the 8a tetrahedral sites and formed a layer with TMO-like spinel structure. The Li, together with part of the Ni, formed a rock salt $Li_xNi_{1-x}O$ phase. Some Ti atoms were found to have diffused into deeper regions of the LNMO particle and occupied the 16d octahedral sites, leading to a slight lattice distortion. An EDX map of the surface tiny particle has been presented in Figure S6 (Supporting Information), the particle was rich in Ti and Mn, indicating that with longer treatment time, the surface TMO-like phase tend to agglomerate into tiny particles. A schematic illustration of the process is demonstrated in Figure S8 (Supporting Information).

To reveal the impact of the TMO-like phase and surface Ti doping on the electrochemical performance of LNMO samples, charge/discharge measurements were carried out at both room temperature (RT) and 55 °C. **Figure 6**a shows the cyclic stability of the samples at a current density of 0.5C under RT. Bare LNMO shows an initial discharge capacity of 116 $mAhg^{-1}$. The plateau at 4.0 V corresponds to the redox couple of Mn^{3+}/Mn^{4+} and it provides ≈25% of the capacity, indicating that there exists a large amount of oxygen deficiencies in the lattice and the LNMO is in the phase of nonstoichiometric $Fd\bar{3}m$ crystallographic structure, which will lead to severe Jahn–Teller distortion that has an onset voltage of 4 V. However, after 350 charge/discharge cycles, its capacity retention was only 74.1%. Besides, the performance of LNMO/25TiO_2 without post-annealing treatment has been studied and shown in Figure S8 (Supporting Information). An initial discharge of only 80 $mAhg^{-1}$ was observed in the LNMO/25TiO_2 sample even though the stability

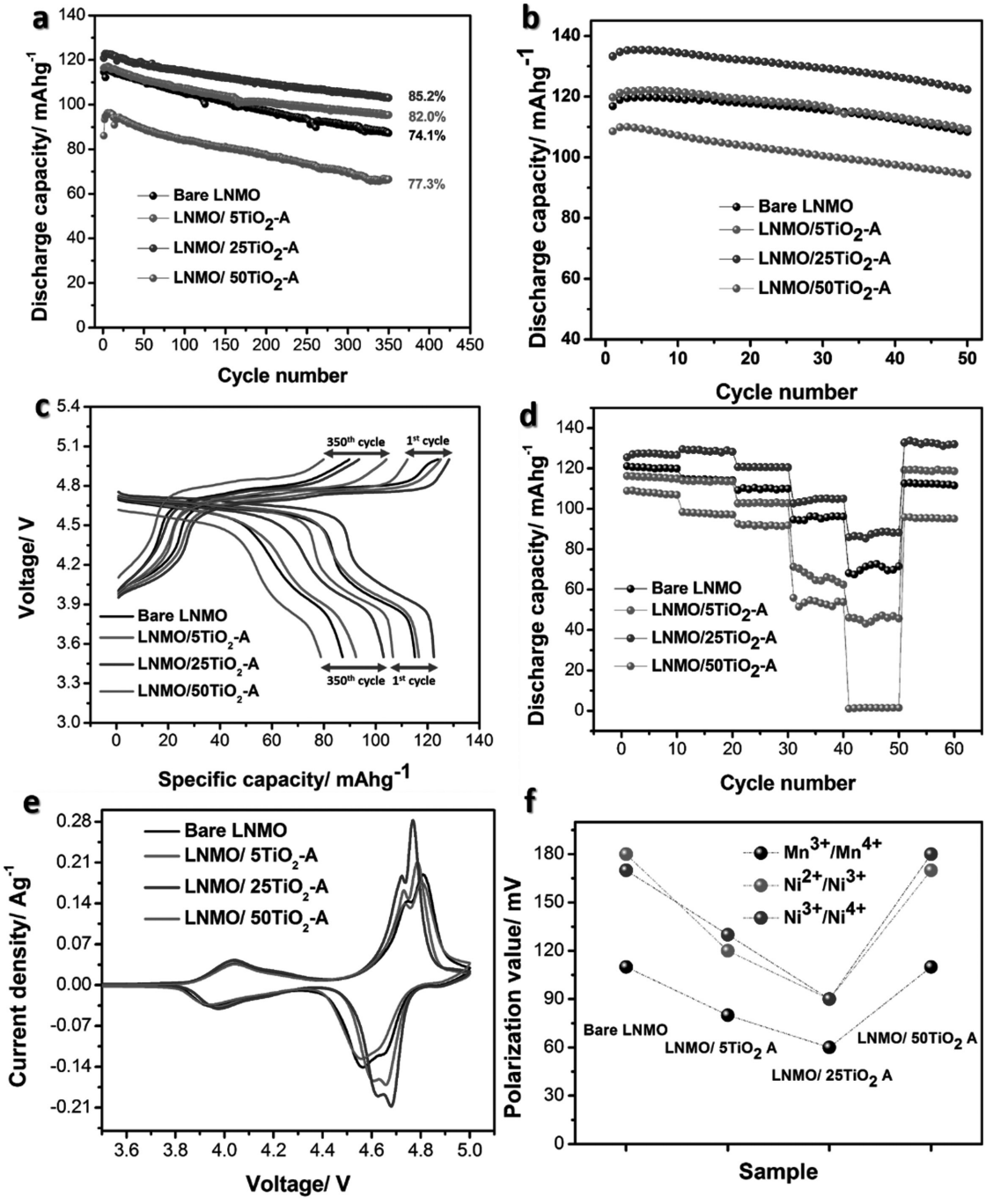

Figure 6. a) Stability test at 0.5C under room temperature; b) stability test at 0.5C under 55 °C; c) 1st and 350th charge/discharge curves under RT; d) rate capability test at 0.1, 0.5, 1, 2, 5, and 0.1C under RT; e) CV curves of the first cycle normalized by active materials weight; f) plots of the polarization potentials of the Mn^{3+}/Mn^{4+}, Ni^{2+}/Ni^{3+}, and Ni^{3+}/Ni^{4+} redox couples calculated based on the CV curves; all of the spectra are based on sample: bare LNMO, LNMO/5TiO_2A, LNMO/25TiO_2A, and LNMO/50TiO_2A.

also reached 85.2%. The inferior performance of LNMO/25TiO_2 is probably due to the insulating nature of TiO_2, which could hamper the Li ions and electron transportation, as schematically shown in Figure S10d (Supporting Information).[53] In contrast, the LNMO/25TiO_2A sample shows apparent improvement. The sample demonstrates increased discharge capacity as well as good stability with 85.2% capacity retention after 350 cycles, 10% higher than that of the bare LNMO. The improved capacity of LNMO/25TiO_2A compared with LNMO/25TiO_2 also suggests that the new surface formed after annealing has a better conductivity than amorphous TiO_2. Such improved kinetics can be presumably ascribed to the 8a tetrahedral vacancies in the TMO-like spinel phase, which can improve the Li ion diffusion rate compared to pure amorphous TiO_2 coating.[54,55]

Coulombic efficiencies shown in Figure S12 (Supporting Information) also reveal that the electrolyte decomposition of the LNMO/25TiO_2A is much less severe than the bare LNMO. These results indicate that surface modification helps to suppress the side reactions between the LNMO particles and the electrolyte. Despite that the TMO-like phase may also be dissolvable in the electrolyte, the stronger Ti—O bond should enable much higher resistivity against the electrolyte than bare LNMO and it is capable of producing a more stable cathode/electrolyte interfacial layer.[56–58] The LNMO/5TiO_2A sample shows slightly improved capacity, but higher capacity retention than the bare LNMO after 350 cycles. In contrast, when the TiO_2 cycle number was increased to 50, the capacity in the LNMO/50TiO_2A sample dropped immediately with only 87 $mAhg^{-1}$ initial discharge capacity, the stability is lower than the bare LNMO or the samples with 5 and 25 ALD cycles either. This capacity drop reveals that the surface structure of the excessive TiO_2 coating on LNMO followed by annealing does not benefit the performance at all and could be ascribed to (1) the lattice distortion caused by overwhelming Ti substitution, as has been observed in bulk doping studies;[28] (2) the increasing amount of the impurity $Li_xNi_{1-x}O_y$ rock salt phase; (3) overwhelming number of Ti^{4+} ions and Mn^{2+} that replace the Li^+ ions on 8a sites;[56] and (4) too much soluble Mn^{2+}.

Moreover, the same test carried out under 55 °C is shown in Figure 6b, it can be seen that all of the capacity fading rates are rather close, this may be due to the fierce side reactions under such high operating temperature. Nevertheless, the discharge capacity follows the same trend as the test conducted under RT, the LNMO/25TiO_2A sample shows even more remarkable improvement with an initial discharge capacity of over 130 $mAhg^{-1}$. The reason for this capacity improvement will be discussed below. It is reasonable that the overall capacity obtained under 55 °C is higher than that of the room temperature because the kinetics of the lithium ions is much more vigorous. The 1st and 350th charge/discharge curves displayed in Figure 6e reveal that the capacity mainly originates from three redox couples, Mn^{3+}/Mn^{4+} at 4 V, Ni^{2+}/Ni^{3+} at 4.6 V, and Ni^{3+}/Ni^{4+} at 4.7 V. Rate capability of the samples is shown in Figure 6d, it can be seen that the LNMO/25TiO_2A sample shows the best performance as well. More than 90 $mAhg^{-1}$ discharge capacity can still be maintained under 5C, whereas LNMO/50TiO_2A shows no capacity at all under this current density. In addition, LNMO/25TiO_2 shows a worse rate capability compared with the LNMO/25TiO_2A sample as shown in Figure S10 (Supporting Information).

In order to further elucidate the redox couples, CV tests were also conducted under RT on these samples. The CV redox peaks support the charge/discharge curves observed in Figure 6c, where redox couples of Mn^{3+}/Mn^{4+} at 4 V, Ni^{2+}/Ni^{3+} at 4.6 V, and Ni^{3+}/Ni^{4+} at 4.7 V are clearly revealed. Also, the normalized intensity of the redox peaks fits well with the trend of the discharge capacities in Figure 6a. The potential polarizations of the redox couples are plotted in Figure 6f, the LNMO/25TiO_2A sample shows the lowest polarization in all of the three redox couples, demonstrating the optimized kinetics of the surface structure. The abovementioned electrochemical studies reveal that the controlled growth of the TMO-like phase is essential to the performance of LNMO, 25 ALD cycle number has demonstrated the most promising performance.

In an effort to understand the improved discharge capacity of the LNMO/25TiO_2A sample, electrochemical impedance spectra (EIS) were collected on both the bare LNMO and the LNMO/25TiO_2A samples after charging to 5 V and holding for 3 h. The EIS of the two charged cells of bare LNMO/Li and LNMO/25TiO_2A/Li samples are shown in **Figure 7**a, two semicircles from high to medium frequency and one inclined line at low frequency can be observed. The simulated equivalent circuit is presented as an inset. The R_Ω stands for the Ohmic resistance that arose from the electrolyte, separator, and other components. The semicircle in the high-frequency range represents the lithium diffusion across the surface film, simulated as a resistor R_s and a constant phase element (CPE); the semicircle in the medium frequency range shows the charge transfer reaction composed of a resistor R_{ct} and another CPE; the inclined line is interpreted as the finite length Warburg impedance. In this case, the value of R_s stands for the solid electrolyte interphase (SEI) resistance and R_{ct} epitomizes the likely phase transformation on the surface of LNMO after initial charging. It can be seen that the bare LNMO shows an R_{ct} value of 58.9 Ω, whereas the LNMO/25TiO_2A sample shows only 9.0 Ω. Lithium diffusion pathway in the spinel structured LNMO is illustrated

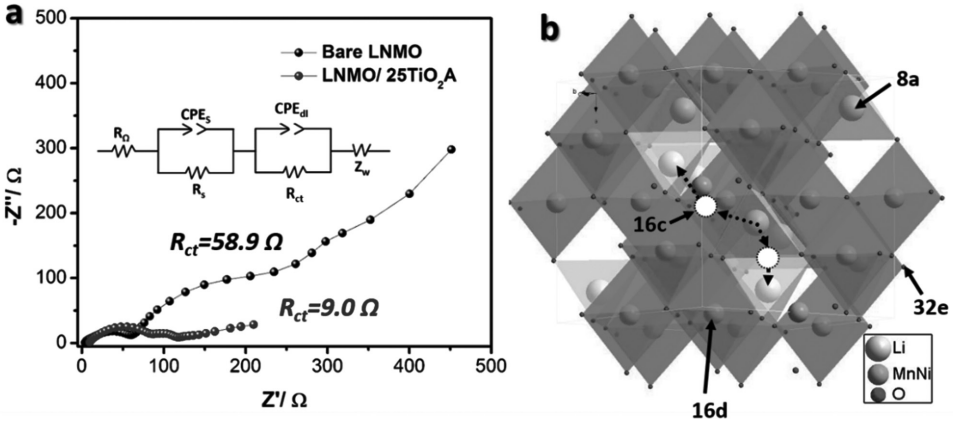

Figure 7. a) EIS of bare LNMO and LNMO/25TiO_2A after initial charge to 5 V; inset: an equivalent-circuit simulation model; b) structure of LNMO showing the lithium ions diffusion path.

in Figure 7b, the lithium ions hop into adjacent empty 16c octahedral sites and then migrate into the next 8a tetrahedral site. Huang and co-workers reported that the surface of LNMO will transform into a Mn_3O_4-like structure during the first charge due to cation migration to the 8a tetrahedral sites, subsequent cation migration from 16d sites into the empty 16c octahedral sites leads to the formation of rock salt-like phase that extends to the interior part of the particles, therefore, the occupation of the empty 16c sites by transition metals will result in severe impedance buildup. They also suggested that preoccupation of the lithium tetrahedral sites with a small amount of insoluble ions can stabilize the structure.[59] In this study, we have validated this assumption by using Ti to occupy the tetrahedral sites. Hence, the formation of the TMO-like phase at the surface region after annealing with Ti substituting into the 8a tetrahedral site should play a key role in inhibiting the structural evolution of the LNMO cathode material during cycling.

The significant impedance difference between the above-mentioned samples reveals that the presence of Ti in tetrahedral sites helps to prevent the LNMO cathode material from the surface structural transformation into a Mn_3O_4-like phase and subsequent formation of a rock salt structure, such modification mitigates the impedance buildup that happens at the initial charge process, this explains why the LNMO/25TiO_2A sample shows higher capacity than bare LNMO under both RT and 55 °C.

In order to further unveil the phase transformation mechanism and the change of surface chemical states upon charging/discharging, the bare LNMO and LNMO-25TiO_2A samples were characterized using soft XANES and the results are shown in **Figure 8**a–d. Mn, Ni $L_{3,2}$-edges and O K-edges of the bare LNMO, LNMO/25TiO_2A, and electrochemically cycled bare LNMO and LNMO/25TiO_2A were recorded. Standard MnO, Mn_2O_3, and MnO_2 were also studied and their Mn $L_{3,2}$ XANES spectra are shown in Figure S11b (Supporting Information); it can be seen that the relative intensity of the peaks correlates well with the oxidation state of the corresponding Mn oxides, which is in accordance with the EELS results shown before. Figure 8a shows the Mn $L_{3,2}$ edge XANES spectra of the referred samples. It can be seen that the samples before electrochemical cycling, whether bare or modified, show predominantly Mn^{4+} feature, with the presence of a small amount of Mn^{3+}, this is in correspondence with the electrochemical tests, where extra plateau at around 4.0 V was observed. A closer scrutiny reveals that the LNMO/25TiO_2A sample has extra shoulders at lower photon energy, this also proves the presence of Mn^{2+} and this is in agreement with the EELS results. Since this sample has a thin layer of TiO_2 with only 25 ALD cycles, the change in the peak feature is not as obvious as what was observed from the EELS results. Nevertheless, the Mn $L_{3,2}$ edge XANES shows a significant change after electrochemical cycling, the majority of the Mn ions are in the state of 2+ and, strikingly, the LNMO/25TiO_2A sample shows much more Mn^{4+} feature than the bare LNMO. A similar phenomenon has also been found in our previous work using $FePO_4$ as coating material to protect the LNMO surface.[60] We can therefore conclude that the presence of the TMO-like phase prevents the Mn in the LNMO from being heavily reduced so that more stable performance can be retained after the electrochemical cycling process.[61,62] Mn $L_{3,2}$-edge XANES spectra collected at FLY mode shown in Figure S11c (Supporting Information) indicate that such reduction does not occur in the bulk. The Ni $L_{3,2}$-edge XANES spectra are shown in Figure 8b, it is apparent that the Ni does not show any changes in any of the samples, this is because Ni^{2+} is already in low valence state.[63] The F K-edges of the cycled bare LNMO and cycled LNMO/25TiO_2-A have also been shown in Figure S11d (Supporting Information), peaks other than the poly(vinylidene fluoride) (PVdF) have emerged in the cycled bare LNMO, which can be assigned to the hydrolysis products of $LiPF_6$. In addition, the sharp peaks at around 710–730 eV assigned to the $L_{3,2}$ edges of Fe in the cycled bare LNMO indicate that the HF amount was very high that even the coin cell cases were corroded. As has been mentioned before, total electron yield (TEY) mode has a detection depth of ≈5 nm, and this range falls into the thickness of the SEI, so the Mn, Ni $L_{3,2}$-edge XANES spectra of the cycled samples obtained in TEY mode also contain information from the SEI.

Kostecki and co-workers proved that the transition metals mainly exist as fluorides and/or organic salts such as oxalate in the SEI layer,[64] indicating the absence of Me—O (Me = Mn, Ni) bonds. Therefore, the O K-edge XANES was collected to understand the composition of the SEI, as shown in Figure 8c where O K-edge XANES spectra before electrochemical cycling show five features, labeled C, E, F, G, and H. Features C and E in the pre-edge regions represent the excitation of O 1s electron to the hybridization of the O 2p with the transition metals 3d orbitals, and are believed to be related to t_{2g} and e_g symmetry, respectively. The broader peaks G and H are due to the hybridization of the O 2p with the transition metals 4sp orbitals.[65,66] It is noticed that feature F appears only in the LNMO/25TiO_2A sample. Actually the O K-edge threshold of Ti—O bonds appears at higher photon energy than Mn—O as has been discussed by F. de Groot,[65] therefore, the feature F corresponds to the e_g symmetry of Ti—O and its t_{2g} symmetry overlaps with the Mn—O and Ni—O e_g symmetry, that is the reason why the intensity of feature E appears to be much higher than feature C after post-annealing. The feature F can be seen in the FLY spectra as well, implying that the Ti—O hybridization exists in rather high depth, which is consistent with the EELS result discussed above. The samples were electrochemically cycled and dissembled so as to understand the oxygen species in the SEI layer.

The TEY spectra of the electrode samples show drastic difference after electrochemical cycling. The bare LNMO shows mostly weak peaks like B and D, they are assigned to the organic compounds in the SEI, whereas in the LNMO/25TiO_2A sample, features E, G, and H still exist. These features are assigned to the hybridization of O 2p and Ni 3d orbitals, the 3d electron configuration of Ni^{2+} is $t_{2g}^6e_g^2$, where the 3 t_{2g} orbitals have been fully filled by electrons, therefore, no t_{2g} peak is expected in Ni^{2+} $L_{3,2}$ edges, that is why only peak E is observed in the pre-edge regions. Ni—O bonds are extremely weak when the LNMO is charged to high voltage since Ni^{4+} is highly electron-depleted, its catalytic effect facilitates the electrolyte decomposition.[35] We can therefore conclude that the transition metal dissolution in the electrochemically cycled bare LNMO sample is so intense that none of the surface Mn or Ni were in the form of oxides any more, whereas Ni—O bonds still exist in the

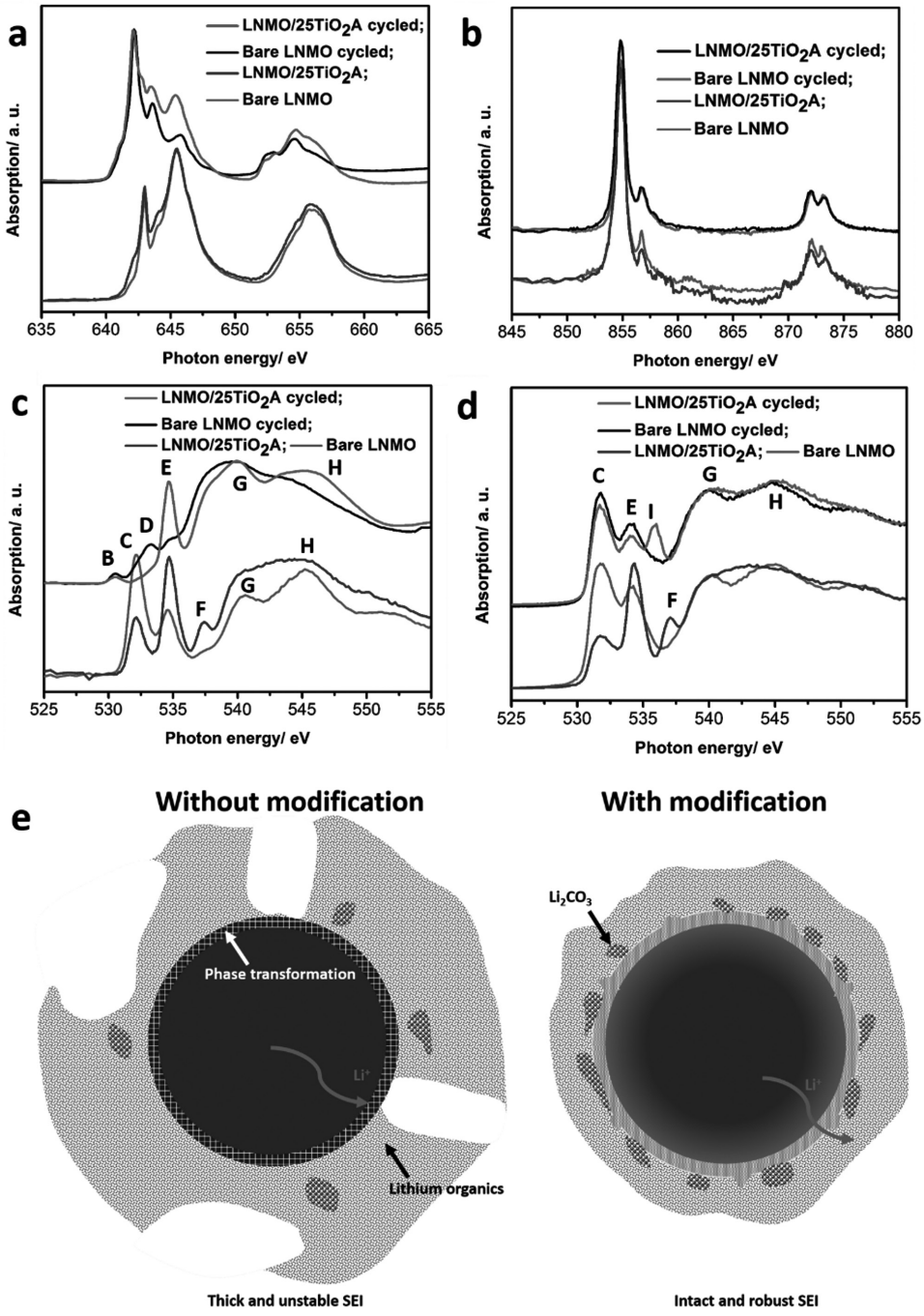

Figure 8. XANES spectra of the bare LNMO, LNMO/25TiO_2A, and bare LNMO after 350 charge/discharge cycles and LNMO/25TiO_2A after 350 charge/discharge cycles in a) Mn $L_{3,2}$-edges collected at TEY mode; b) Ni $L_{3,2}$-edges collected at TEY mode; c) O K-edges collected at TEY mode; d) O K-edges collected at FLY mode; e) schematic illustration of the bare LNMO and LNMO/25TiO_2A after 350 charge/discharge cycles.

LNMO/25TiO_2A sample since the incorporation of Ti^{4+} can possibly strengthen the Ni—O bond, as has been observed in Cabana's work of incorporating Mg^{2+} into the surface of LNMO.[35] Another possibility is that the rock salt $Li_xNi_{1-x}O$ phase remains on the surface, it acted as a protection agent against HF attack. Taking a look at the FLY spectra, one can find that the features C, E, F, G, and H still exist, indicating that the loss of Me—O bonds mainly happens on the surface. The area of peaks C and E is lower in the cycled LNMO/25TiO_2A than the cycled bare LNMO, indicating the presence of less oxygen 2p hybridization with TM 3d orbitals in the bulk, which complies with the reduction of Mn. A new peak "I" appears in the electrochemically cycled LNMO/25TiO_2A sample. This intensive peak has also been reported in many references where electrolyte additives were studied. It can be assigned to the π^* orbital of the C=O bond in Li_2CO_3.[67] Li_2CO_3 is a well-known favorable SEI

component since it helps create a more robust and dense SEI layer, this can be another reason of the improved stability.[68–70] The Li_2CO_3 signal can be observed in FLY spectra but not TEY spectra, indicating that it mainly locates at the "inner" layer of the SEI which is closer to the surface of the electrode materials, probably because that Li_2CO_3 forms at the beginning of the electrochemical cycling.

To summarize the results above, we depict a schematic illustration in Figure 8e. The presence of spinel TMO-like phase and Ti occupation of octahedral sites in LNMO help create an SEI with more Li_2CO_3, strengthen the Ni—O bonds and prevent severe Mn reduction and dissolution during electrochemical cycling. The Li_2CO_3 helps build more robust SEI. The suppression of the reduction of Mn and the stronger Ni—O interaction help retain better surface consistency upon electrochemical cycling.

We have carried out a systematic study of the post-annealing effect on the performance of ALD-TiO_2 coated LNMO. It is found that the surface of the LNMO undergoes several changes during the process: (1) partial Ti substitution of 8a Li tetrahedral sites, forming a TMO-like phase; (2) Li and Ni extrusion, forming rock salt $Li_xNi_{1-x}O$ phase; (3) octahedrally coordinated Mn/Ni replacement by Ti in deeper region, resulting in slight doping of LNMO; (4) aggregation of the TMO-like phase into tiny particles. Electrochemical studies reveal that the formation of the TMO-like spinel phase on the surface through the substitution of Ti in the 8a tetrahedral sites will help undermine the impedance buildup resulting from the continuous formation of rock salt structure during electrochemical cycling. In addition, the presence of the substituted Ti strengthens the Ni—O bond. The TMO-like phase helps form an SEI with more desirable Li_2CO_3 and hampers the reduction of Mn after electrochemical cycling. More importantly, the effect of Ti substitution highly depends on the ALD cycle number, 25 ALD cycle appears to produce the optimal thickness that yields improved stability, Coulombic efficiency, discharge capacity, and rate capability. Nevertheless, other factors such as annealing time and temperature are worthwhile to be further studied. This work has paved the path to controlled manipulation of surface structures on cathode materials, provided a novel explanation to the role of surface modification, and extended the practice of ALD technique in LIBs and related research.

Experimental Section

Materials Preparation: The LNMO powders were purchased from Daejung Energy Materials Co. Ltd., South Korea. ALD of TiO_2 was performed at 150 °C in a Savannah 100 ALD system (Ultratech/Cambridge Nanotech) by using titanium(IV) isopropoxide (TTIP, $Ti[OCH(CH_3)_2]_4$, Sigma Aldrich, 97%) and distilled water (H_2O) as precursors. The source temperature for TTIP was 85 °C, while H_2O was kept at RT. N_2 gas was used as the carrying and purging gas, at a flow rate of 20 sccm. Each ALD cycle of TiO_2 was executed with the following steps: (1) 1 s pulse of TTIP; (2) 3 s extended exposure of TTIP in the reaction chamber; (3) 20 s purge of residual TTIP and any by-products; (4) 1 s pulse of H_2O; (5) 3 s extended exposure of H_2O in the reaction chamber; (6) 20 s purge of residual H_2O and any by-products. The growth process has also been illustrated in Figure S1 (Supporting Information). LNMO powders were dispersed on a stainless steel tray, and then put at the center of the ALD reaction chamber. TiO_2 was deposited on LNMO powders by repeating the above ALD cycles, the corresponding samples are denoted as LNMO/$n$$TiO_2$ where n stands for the ALD cycle number. 5, 25, and 50 cycle numbers were chosen as the performance study parameter. In order to better characterize the consequence of the TiO_2 reaction with LNMO upon post-treatment, 250 ALD cycle number was used for Ti-related structural studies.

In the post-treatment process, the LNMO/$n$$TiO_2$ samples were annealed in air under 810 °C for 6 h followed by slow cooling to RT within 10 h. The treated samples were named as LNMO/$n$$TiO_2$A. All of the bare LNMO samples studied were treated under the same conditions as well to make the results comparable.

Characterization Methods: The morphology of the samples was characterized by a Hitachi S-4800 field emission scanning electronic microscopy (FESEM) and a JEOL 2010F field emission TEM. The XRD patterns were collected on a Bruker D8 Advance Diffractometer using Cu Kα radiation at 40 kV and 40 mA. The stoichiometry of the as-purchased LNMO was determined by an inductively coupled plasma optical emission spectrometer (ICP-OES, Vista Pro Axial, Varian, Australia). The soft XANES measurements with both TEY and FLY modes at the Mn $L_{3,2}$-edges, Ni $L_{3,2}$-edges, and O K-edge were collected at the Spherical Grating Monochrometer (SGM) beamline with a photon energy of 250–2000 eV at the Canadian Light Source. The Ti K-edge XANES was collected at the Soft X-ray Microcharacterization Beamline (SXRMB) at the Canadian Light Source.

For the electron microscope (EM) specimen preparation, the pristine and LNMO/250TiO_2 powder samples were suspended on the copper grids for EM characterization. The LNMO/250TiO_2A specimen was prepared using a Zeiss NVision 40 dual beam focused ion beam (FIB)/SEM for a detailed structural analysis. EELS and the STEM characterization were carried out on an aberration-corrected (probe and image-forming lenses) FEI Titan Cubed 80–300 kV microscope equipped with a Gatan Image Filter Quantum-965 spectrometer operated at 200 kV. EELS spectra were recorded with a 0.25 eV/channel dispersion of the spectrometer. The HAADF-STEM image acquired with a HAADF detector is also called a "Z-contrast" image, whereby the image intensity is proportional to the atomic number ($\propto Z^{1.7}$) of the elements present in the material.

Electrochemical Measurements: The LNMO powders were uniformly mixed with acetylene black (AB) and poly(vinylidene fluoride) in a ratio of 8:1:1 in N-methyl-pyrrolidione (NMP) as solvent. The slurry was then pasted onto aluminum foils and dried at 80 °C overnight under vacuum. The electrode was subsequently cut into round shape with a diameter of 12 cm and assembled into a CR-2032 coin cell in a glove box with moisture and oxygen being controlled below 1.0 ppm. Lithium metal was used as the counter electrode in the coin cells. The electrolyte was composed of 1 M $LiPF_6$ dissolved into ethylene carbonate (EC) and dimethyl carbonate (DMC) in a 1:1 volume ratio (BASF Corp.). Celgard K2045 was used as the separator. Cyclic voltammetry (CV) was performed on a Bio-Logic multichannel potentiostat 3/Z (VMP3) with a scanning rate of 0.1 mV s^{-1} and a potential range of 3.5–5.0 V (vs Li/Li^+) at RT. Galvanostatic charge/discharge test was carried out on an Arbin BT 2000 at various current densities between 3.5 and 5.0 V (vs Li/Li^+). The cyclic stability test was done at a current density of 0.5 C (1C = 147 mAg^{-1}) under both RT and 55 °C. The tested cells were dissembled in the glove box and the cathode sheets were collected and thoroughly washed with DMC for several times and kept in a hermetic box for XAS study.

Supporting Information

Supporting Information is available from the Wiley Online Library or from the author.

Acknowledgements

B.X. and H.L. contributed equally to this work. This research was supported by the Natural Science and Engineering Research Council of

Canada (NSERC), the Canada Research Chair Program (CRC), General Motors R&D Center (GM), the Canada Foundation for Innovation (CFI), Canadian Light Source (CLS) at the University of Saskatchewan, the Canadian Centre for Electron Microscopy (CCEM) at McMaster University, and the University of Western Ontario (UWO).

Conflict of Interest

The authors declare no conflict of interest.

Keywords

atomic layer deposition, $LiNi_{0.5}Mn_{1.5}O_4$, surface structure, $TiMn_2O_4$-like spinel, TiO_2

Received: July 6, 2017
Revised: August 22, 2017
Published online:

[1] J. B. Goodenough, K. S. Park, *J. Am. Chem. Soc.* **2013**, *135*, 1167.
[2] A. Manthiram, K. Chemelewski, E. S. Lee, *Energy Environ. Sci.* **2014**, *7*, 1339.
[3] A. Kraytsberg, Y. Ein-Eli, *Adv. Energy Mater.* **2012**, *2*, 922.
[4] Y. Shao-Horn, S. A. Hackney, A. J. Kahaiana, K. D. Kepler, E. Skinnerac, J. T. Vaugheya, M. M. Thackeray, *J. Power Sources* **1999**, *81*, 496.
[5] T. Eriksson, T. Gustafsson, J. O. Thomas, *Electrochem. Solid State* **2002**, *5*, A35.
[6] K. Y. Chung, K. B. Kim, *Electrochim. Acta* **2004**, *49*, 3327.
[7] P. Arora, *J. Electrochem. Soc.* **1998**, *145*, 3647.
[8] K. Xu, *Chem. Rev.* **2004**, *104*, 4303.
[9] D. H. Jang, *J. Electrochem. Soc.* **2004**, *143*, 2204.
[10] F. Lin, I. M. Markus, D. Nordlund, T.-C. Weng, M. D. Asta, H. L. Xin, M. M. Doeff, *Nat. Commun.* **2014**, *5*, 3529.
[11] J. Cho, Y. J. Kim, B. Park, *Chem. Mater.* **2000**, *12*, 3788.
[12] J. S. Kim, C. S. Johnson, J. T. Vaughey, S. A. Hackney, K. A. Walz, W. A. Zenltner, M. A. Anderson, M. M. Thackeray, *J. Electrochem. Soc.* **2004**, *151*, A1755.
[13] S. T. Myung, K. Izumi, S. Komaba, Y. K. Sun, H. Yashiro, N. Kumagai, *Chem. Mater.* **2005**, *17*, 3695.
[14] Z. Wang, E. Liu, C. He, C. Shi, J. Li, N. Zhao, *J. Power Sources* **2013**, *236*, 25.
[15] Y. Kim, N. J. Dudney, M. Chi, S. K. Martha, J. Nanda, G. M. Veith, C. Liang, *J. Electrochem. Soc.* **2013**, *160*, A3113.
[16] H. G. Song, K. S. Park, Y. J. Park, *Solid State Ionics* **2012**, *225*, 532.
[17] J. Chong, S. Xun, J. Zhang, X. Song, H. Xie, V. Battaglia, R. Wang, *Chem. Eur. J.* **2014**, *20*, 7479.
[18] J. Zheng, M. Gu, J. Xiao, B. J. Polzin, P. Yan, X. Chen, C. Wang, J.-G. Zhang. *Chem. Mater.* **2014**, *26*, 6320.
[19] H. J. Lee, Y. J. Park, *Solid State Ionics* **2013**, *230*, 86.
[20] S. T. Myung, S. Komaba, N. Kumagai, *J. Electrochem. Soc.* **2001**, *148*, A482.
[21] M. H. Liu, H. T. Huang, C. M. Lin, J. M. Chen, S. C. Liao, *Electrochim. Acta* **2014**, *120*, 133.
[22] K. R. Chemelewski, W. Li, A. Gutierrez, A. Manthiram, *J. Mater. Chem. A* **2013**, *1*, 15334.
[23] S. J. R. Prabakar, S. C. Han, S. P. Singh, D. K. Lee, K. S. Sohn, M. Pyo, *J. Power Sources* **2012**, *209*, 57.
[24] H. Wang, T. A. Tan, P. Yang, M. O. Lai, L. Lu, *J. Phys. Chem. C* **2011**, *115*, 6102.
[25] J. Liu, A. Manthiram, *J. Phys. Chem. C* **2009**, *113*, 15073.
[26] M. Lin, S. H. Wang, Z. L. Gong, X. K. Huang, Y. Yang, *J. Electrochem. Soc.* **2013**, *160*, A3036.
[27] A. Höweling, S. Glatthaar, D. Nötzel, J. R. Binder, *J. Power Sources* **2015**, *274*, 1267.
[28] R. Alcántara, M. Jaraba, P. Lavela, J. L. Tirado, *Chem. Mater.* **2003**, *15*, 2376.
[29] J. H. Kim, S. T. Myung, C. S. Yoon, I. H. Oh, Y. K. Sun, *J. Electrochem. Soc.* **2004**, *151*, A1911.
[30] K. Y. Chung, W. S. Yoon, H. S. Lee, X.-Q. Yang, J. McBreen, B. H. Deng, X. Q. Wang, M. Yoshio, R. Wang, J. Gui, M. Okada, *J. Power Sources* **2005**, *146*, 226.
[31] J. Cho, Y. J. Kim, B. Park, *J. Electrochem. Soc.* **2001**, *148*, A1110.
[32] J. Cho, T. J. Kim, B. Park, *J. Electrochem. Soc.* **2002**, *149*, A288.
[33] S. Verdier, L. El Ouatani, R. Dedryvère, F. Bonhomme, P. Biensan, D. Gonbeau, *J. Electrochem. Soc.* **2007**, *154*, A1088.
[34] L. Dahéron, R. Dedryvère, H. Martinez, D. Flahaut, M. Ménétrier, C. Delmas, D. Gonbeau, *Chem. Mater.* **2009**, *21*, 5607.
[35] G. Alva, C. Kim, T. Yi, J. B. Cook, L. Xu, G. M. Nolis, J. Cabana, *J. Phys. Chem. C* **2014**, *118*, 10596.
[36] J. H. Shim, S. Lee, S. S. Park, *Chem. Mater.* **2014**, *26*, 2537.
[37] X. Li, J. Liu, M. Banis, A. Lushington, R. Li, M. Cai, X. Sun, *Energy Environ. Sci.* **2014**, *7*, 768.
[38] X. Li, J. Liu, X. Meng, Y. Tang, M. Banis, J. Yang, Y. Hu, R. Li, M. Cai, X. Sun, *J. Power Sources* **2014**, *247*, 57.
[39] C. Marichy, M. Bechelany, N. Pinna, *Adv. Mater.* **2012**, *24*, 1017.
[40] D. Qian, B. Xu, M. Chi, Y. S. Meng, *Phys. Chem. Chem. Phys.* **2014**, *16*, 14665.
[41] M. E. Arroyo-de Dompablo, C. Marianetti, A. Van der Ven, G. Ceder, *Phys. Rev. B* **2011**, *63*, 144107.
[42] J. H. Kim, N. P. W. Pieczonka, Y. K. Sun, B. R. Powell, *J. Power Sources* **2014**, *262*, 62.
[43] M.-L.-P. Le, P. Strobel, F. Alloin, T. Pagnier, *Electrochim. Acta* **2010**, *56*, 592.
[44] A. Erbil, I. G. Cargill, R. Frahm, R. F. Boehme, *Phys. Rev. B* **1988**, *37*, 2450.
[45] J. Jaklevic, J. A. Kirby, M. P. Klein, A. S. Robertson, G. S. Brown, P. Eisenberger, *Solid State Commun.* **1977**, *23*, 679.
[46] T. Hiratoko, A. Yoshiasa, T. Nakatani, M. Okube, A. Nakatsuka, K. Sugiyama, *J. Synchrotron Radiat.* **2013**, *20*, 641.
[47] D. T. Murphy, S. Schmid, J. R. Hester, P. E. Blanchard, W. Miiller, *Inorg. Chem.* **2015**, *54*, 4636.
[48] G. A. Lager, T. Armbruster, F. K. Ross, F. J. Rotella, J. D. Jorgensen, *J. Appl. Crystallogr.* **1989**, *14*, 261.
[49] J. Lu, C. Zhan, T. Wu, J. Wen, Y. Lei, A. J. Kropf, H. Wu, D. J. Miller, J. W. Elam, Y.-K. Sun, X. Qiu, K. Amine, *Nat. Commun.* **2014**, *5*, 5693.
[50] K. Petrov, R. M. Rojas, P. J. Alonso, J. M. Amarilla, M. G. Lazarraga, J. M. Rojo, *Solid State Sci.* **2005**, *7*, 277.
[51] J. H. Paterson, O. L. Krivanek, *Ultramicroscopy* **1990**, *32*, 319.
[52] G. S. Henderson, X. Liu, M. E. Fleet, *Miner. Mag.* **2003**, *67*, 597.
[53] Y. S. Jung, A. S. Cavanagh, L. A. Riley, S. H. Kang, A. C. Dillon, M. D. Groner, S. M. George, S. H. Lee, *Adv. Mater.* **2010**, *22*, 2172.
[54] Z. Moorhead-Rosenberg, A. Huq, J. B. Goodenough, A. Manthiram, *Chem. Mater.* **2015**, *27*, 6934.
[55] K. Hoang, *J. Mater. Chem. A* **2014**, *2*, 18271.
[56] S. Wang, J. Yang, X. Wu, Y. Li, Z. Gong, W. Wen, M. Lin, J. Yang, Y. Yang, *J. Power Sources* **2014**, *245*, 570.
[57] R. Chen, R. Heinzmann, S. Mangold, V. S. K. Chakravadhanula, H. Hahn, S. Indris, *J. Phys. Chem. C* **2014**, *118*, 12608.
[58] J. Kim, N. P. W. Pieczonka, P. Lu, Z. Liu, R. Qiao, W. Yang, M. M. Tessema, Y.-K. Sun, B. R. Powell, *Adv. Mater. Interfaces* **2015**, *2*, 1500109.

[59] M. Lin, L. Ben, Y. Sun, H. Wang, Z. Yang, L. Gu, X. Yu, X.-Q. Yang, H. Zhao, R. Yu, M. Armand, X. Huang, *Chem. Mater.* **2015**, *27*, 292.
[60] B. Xiao, J. Liu, Q. Sun, B. Wang, M. Banis, D. Zhao, Z. Wang, R. Li, X. Cui, T.-K. Sham, X. Sun, *Adv. Sci.* **2015**, *2*, 1500022.
[61] N. P. W. Pieczonka, Z. Liu, P. Lu, K. L. Olsen, J. Moote, B. R. Powell, J.-H. Kim, *J. Phys. Chem. C* **2013**, *117*, 15947.
[62] C. Zhan, J. Lu, J. Kropf, T. Wu, A. N. Jensen, Y.-K. Sun, X. Qiu, K. Amine, *Nat. Commun.* **2013**, *4*, 2437.
[63] R. Qiao, Y. Wang, P. Olalde-Velasco, H. Li, Y. S. Hu, W. Yang, *J. Power Sources* **2015**, *273*, 1120.
[64] A. Jarry, S. Gottis, Y.-S. Yu, J. Roque-Rossel, C. Kim, J. Cabana, J. Kerr, R. Kostecki, *J. Am. Chem. Soc.* **2015**, *137*, 3533.
[65] F. de Groot, M. Grioni, J. Fuggle, J. Ghijsen, G. Sawatzky, H. Petersen, *Phys. Rev. B* **1989**, *40*, 5715.
[66] J. Zhou, D. Hong, J. Wang, Y. Hu, X. Xie, H. Fang, *Phys. Chem. Chem. Phys.* **2014**, *16*, 13838.
[67] C. Yogi, D. Takamatsu, K. Yamanaka, H. Arai, Y. Uchimoto, K. Kojima, I. Watanabe, T. Ohta, Z. Ogumi, *J. Power Sources* **2014**, *248*, 994.
[68] S. Shi, P. Lu, Z. Liu, Y. Qi, L. G. Hector, H. Li, S. J. Harris, *J. Am. Chem. Soc.* **2012**, *134*, 15476.
[69] B. R. Wu, Y. H. Ren, D. B. Mu, X. J. Liu, G. C. Yang, F. Wu, *RSC Adv.* **2014**, *4*, 10196.
[70] L. Yang, B. Ravdel, B. L. Lucht, *Electrochem. Solid State* **2010**, *13*, A95.

